Hydrogen photoproduction on TiO$_2$-CuO artificial olive leaves

Juan Martín-Gómez, Jesús Hidalgo-Carrillo, Rafael C. Estévez, Francisco J. Urbano, Alberto Marinas*

Departamento de Química Orgánica, Instituto Universitario de Investigación en Química Fina y Nanoquímica (IUNAN), Facultad de Ciencias, Universidad de Córdoba, Campus de Rabanales, Edificio Marie Curie, E-14071 Córdoba, Spain.

To Prof. Vasile I. Parvulescu, an excellent researcher and even better human being

Abstract

Olive leaves were used as biotemplates to synthesize diverse TiO$_2$-CuO solids. A successful replication of trichomes and internal channels was evidenced by SEM, whereas a good dispersion of Cu and Ti atoms was observed by EDX. The systems consisted in pure anatase titania, with monoclinic CuO detected by XRD and Raman for large copper contents (over 15wt%). XPS evidenced the existence of a TiO$_2$-CuO strong interaction. Incorporation of copper resulted in an enhancement of photocatalytic activity, hydrogen production being 84 times higher with the best TiO$_2$-CuO system than with bare titania. It seems that there is a maximum surface copper content (close to a Cu/(Ti+Cu) mol % value of 17) above which CuO particles could promote electron-hole recombination and/or have a shielding effect thus preventing light absorption by titania. The smaller the CuO crystallite sizes the better their reducibility and the catalytic performance of the systems under solar light irradiation.

Keywords: hydrogen photocatalytic production; photoreforming; glycerol; CuO-TiO$_2$

*Corresponding author. Tel.: +34 957218622; fax: +34 957212066. E-mail address: alberto.marinas@uco.es

1. Introduction

Surface structure of materials can be replicated through the so-called templating method. When biological materials are used as the templates, the synthetic method is usually referred to as biotemplating. Biological materials present several inspiring properties such as sophistication, miniaturization, hierarchical organization, hybridization, resistance and adaptability, derived from selection processes developed over millions of years [1]. Therefore, in recent years, diverse natural materials such as bacteria, viruses, diatoms, insect wings, plant leaves, wood, DNA and proteins have been used as templates to design and synthesize new inorganic materials with a defined structure [2]. In particular, this approach can be used in the synthesis of new photocatalytic materials. Green leaves possess a hierarchical structure which contributes greatly to the capture and transport of light, which favors photosynthesis processes [3,4]. Consequently, replication of such structure in photocatalytic materials could contribute to the improvement in light use and thus on catalytic performance. There are some examples in the literature of biotemplating using plant leaves. Zhou et al. replicated *Anemone vitifolia* Buch. leaf on a ZnO solid and used it for hydrogen generation through ethanol photoreforming, its catalytic performance being higher than that achieved on reference material P25 TiO_2 [5]. Sathu et al. [6] used champa (*Plumeria Magnolia champaca*) tree leaves as templates for ZnO and tested it for benzene to phenol oxidation under UV light. Hashemizadeh et al. [7] replicated *Camellia* leaves morphology on artificial titania leaves. The solid was tested for CO_2 reduction to hydrocarbons under both UV and visible light outperforming P25 TiO_2. In a different approach, Tseng et al. [8] used the nanocasting technique to duplicate the surface structure of leaves of *Xanthosoma sagitifolium* on polyimide films. Subsequent incorporation of

cuprous oxide resulted in a photocatalytic material successfully used in the CO_2 reduction to CO under visible-light illumination.

Olive oil production is of paramount importance in Andalusia, accounting for ca. 37% of world production. Leaves constitute one of the by-products obtained in the olive mill (representing roughly 8wt% of milled olive). In a previous paper, we described the valorization of such olive leaves as biotemplates for a titania catalyst [9]. The solid was tested for hydrogen production through glycerol photoreforming and exhibited an activity 64% and 144% higher than commercial TiO_2 P25 under sunlight and UV, respectively. Titania is the most used photocatalyst due to its optical properties, price, stability, non-toxicity and availability [10,11]. However, its use also has some disadvantages such as a high rate of recombination of the photogenerated electron-hole pairs, which would lead to a low photocatalytic efficiency, and a large band gap (in the 3.0 - 3.2 eV range) which means that it only absorbs in the UV region, which hardly represents 5% of solar radiation. Titania photocatalytic activity could be improved through its modification with metals which could retard electron-hole recombination and extent the light absorption to the visible. For economic reasons, non-noble-metals such as Fe, Cu or Ni are particularly attractive [12–14].

In the present piece of research several TiO_2-CuO systems were synthesized using olive leaves as the template through a modification of our previously-described protocol [9]. The solids were tested for hydrogen production through glycerol photoreforming. Therefore, two by-products from olive oil and biodiesel production (olive leaves and glycerol) were valorized. Moreover, the production of hydrogen from biomass is greener than its obtaining from fossil fuels (typically hydrocarbon steam reforming).

2. Experimental

2.1. Materials

Copper (II) chloride dihydrate (Art Nr. 307483), titanium (III) chloride (Art Nr. 7705-07-9), titanium (IV) isopropoxide (Art Nr. 205273), copper (II) acetate (Art. Nr 326755), ethanol (Art. Nr 107017), and propane-1,2,3-triol (glycerol, Art Nr. P50404) were purchased from Sigma Aldrich. Propan-2-ol (isopropanol) was obtained from Merck (Art Nr. 33539-M) and 37wt% hydrochloric acid (Art Nr 141020) from Panreac. Milli-Q water was used for preparation of solutions. Commercial CuO (Sigma Aldrich Art. Nr 544868) was used for physical mixtures. The solid has a surface area of 11 $m^2 \cdot g^{-1}$ and consist in tenorite with a crystallite size of ca. 17nm [15].

2.2 Synthesis of the catalysts

Catalysts were synthesized using olive leaves as the templates. The synthesis involves a first step consisting in the acid treatment of the leaves to replace Mg^{2+} ions in porphyrin rings by H^+, thus forming pheophytins. Then, those protons are exchanged for Ti^{3+} and/or Cu^{2+} through a treatment with the corresponding chlorides. Finally, Cu^{2+} and/or Ti^{3+} ions act as seeds for the formation of the TiO_2-CuO structure.

Therefore, 20 g of fresh olive leaves were washed, dried and ground. The fragments were then treated with 300mL of an aqueous 5% HCl solution until achieving a yellow-brown color characteristic of pheophytins. The solid was then filtered and separated in 10 fractions of 2g each which would eventually lead to 10 different catalysts belonging to two different series (labelled as IP and Et, respectively). In IP series, five of the fractions were treated with 20 mL of a solution containing 40 mmol of $TiCl_3$/$CuCl_2$ mixtures at 0, 25, 50, 75 and 100 mol % of titanium, respectively. The mixtures were stirred overnight under inert (N_2) atmosphere. The solids were then filtered, dried in a vacuum desiccator at 80ºC

4

and subsequently suspended in 30 mL isopropanol to eliminate water traces. Afterwards, 30 mL isopropanol and 6 mmol titanium isopropoxide were added and the suspension refluxed at 85ºC for 6h. Finally, the solids were filtered, dried and calcined at 550ºC in the furnace for 6h. The solids thus obtained follow the nomenclature CuTi(x:y)|Ti-IP, where x and y refers to the copper:titanium molar ratio in the mixture and Ti-IP indicates the subsequent treatment with the titanium precursor in isopropanol (IP) medium. Therefore, for instance, CuTi(1:3)|Ti-IP and Cu|Ti-IP refers to two systems submitted to an initial treatment with a Cu/Ti 25%/75% or 100%Cu mixture of chloride precursors, respectively, and then titanium isopropoxide dissolved in isopropanol.

The other 5 fractions of 2g each (Et-series catalysts) were treated with 40 mmol of $TiCl_3$ and stirred overnight under inert (N_2) atmosphere. The solids were then filtered, dried in a vacuum desiccator at 80ºC and subsequently suspended in 30mL isopropanol to eliminate water traces. Afterwards, 30 mL of an ethanol absolute solution containing 6 mmol of titanium/copper mixture (0, 25, 50, 75 or 100% of titanium, respectively) were added. The corresponding precursors were copper (II) acetate and titanium (IV) isopropoxide. The suspensions were refluxed at 85ºC for 6h. Finally, the solids were filtered out, dried and calcined at 550ºC in the furnace for 6h. Nomenclature of these solids is Ti|CuTi(x:y)-Et were x and y indicate the molar ratio of copper and titanium precursors in the ethanol (Et suffix) solution. Therefore, for instance, Ti|CuTi(1:1)-Et denotes a solid treated with $TiCl_3$ first and then with an equimolecular mixture of copper acetate and titanium isopropoxide in ethanol media.

2.3 Characterization of the catalysts

Inductively coupled plasma mass spectrometry (ICP-MS) experiments were performed on a PerkinElmer NexION 350X instrument following dissolution of the sample. Atomic spectroscopy standards from Perkin Elmer were used for calibration.

X-ray fluorescence analyses were carried out on sample pellets using a Rigaku tube-above wave-length dispersive X-ray fluorescence ZSX Primus IV spectrometer, equipped with an X-ray tube with 4 kW rhodium anode, a proportional gas flow detector for light elements and a scintillation counter for heavy elements.

Scanning electron microscopy (SEM) and energy-dispersive spectroscopy (EDS) analysis were obtained at the Central Service for Research Support (SCAI) of the University of Córdoba with a JEOL JSM 7800F microscope interfaced to an Oxford Instruments X-max 150 semi-quantitative elemental microanalyzer.

Nitrogen adsorption-desorption isotherms, at the liquid nitrogen temperature, were performed on an Autosorb-iQ-MP/MP-XR device, using the Brunauer-Emmet-Teller (BET) method. Before measurements, all samples were degassed at 120 °C and 0.1 Pa.

XRD analysis were performed on a Bruker D8 Discover with a monochromatic source CuKα1 at λ = 1.54 Å radiation over an angular range of 20–80 ° at a scan speed of 1.45 ° 2Θ·min^{-1}.

Raman spectroscopy was carried out at the Central Service for Research Support (SCAI) of the University of Córdoba on a confocal NRS-5500 Raman spectrometer (Jasco Inc.) with 532 nm laser excitation, L1800 grating and an EMCCD detector. Spectra were taken through 20x objective lens, accumulating 10 scans (10 seconds exposure) with a laser power at sample point of 6.6 mW.

Diffuse reflectance UV-Vis spectra were performed on a Cary 5000 (Varian) UV-Vis-NIR spectrophotometer, using polytetraethylene as reference material. Band gap (Eg) values

were obtained from the plot of the modified Kubelka–Munk function $[F(R) \bullet E]^{1/2}$ versus the energy of the absorbed light E.

X-ray photoelectron spectroscopy (XPS) data was recorded at the Central Service for Research Support (SCAI) of the University of Córdoba on pellets after outgassing the samples to a pressure below 2×10^{-8} Torr at 150 °C. A Leibold–Heraeus LHS10 spectrometer was operated with the AlKα (hv = 1486.6 eV) X-ray source at 120 W and 30 mA using C (1 s) as energy reference (284.6 eV).

Temperature-programmed reduction (TPR) analyses were performed on a Micromeritics AutoChem II chemisorption analyser. 40 mg of catalysts were placed in the sample holder and submitted to an initial oxidation step (synthetic air flow 20mL·min^{-1} at 150ºC during 30min). Then, the gas flow was changed to Ar and the temperature dropped to 50ºC. Finally, the sample was reduced in a 20 mL·min^{-1} H_2/Ar (5:95) flow. Temperature was ramped between 50 and 600° C at 10°C·min^{-1}. The final temperature was kept for 25 min.

2.4. Liquid-phase photocatalytic reactions

The liquid-phase photocatalytic reactions were performed in two different devices using suspensions of 1g·L^{-1} catalyst in 10% (v/v) glycerol in water solutions under inert atmosphere. For experiments under UV light (Figures S1A and S1B), the device consisted in a quartz cylindrical reactor of 11 mL. The reaction was performed under argon atmosphere and was irradiated in a Penn PhD Photoreactor M2 equipped with a LED lamp that emits at 365 nm. The reaction medium consisted of 5 mL of glycerol at 10% (v/v) in water and 5 mg of catalyst, thus leaving 6 mL gas phase reactor head space.

For solar-light experiments, reactions were performed under argon atmosphere in an 8.5 mL cylindrical reactor irradiated with light from a Newport solar simulator furnished with a 150 W xenon lamp (Figures S1C and S1D). The reaction medium consisted of 4 mL of

glycerol at 10% (v/v) in water and 4 mg of catalyst, thus leaving 4.5 mL gas phase reactor head space.

LED lamp emits within a very narrow wavelength (ca. 365±20 nm) whereas emission spectrum of the solar-simulator lamp (re. 6255) can be found elsewhere [16]. Photon fluxes as measured by ferrioxalate actinometry [17] were ca. $1.9 \cdot 10^{-7}$ and $1.9 \cdot 10^{-6}$ Einstein·s^{-1} for solar-simulated light and UV LED irradiation, respectively. In both experimental devices, analyses were performed by sampling 100 microliters with a pressure-lock precision analytical syringe (Valco VICI Precision Syringes, 1 mL, leak-tight to 250 psi) from the head space of the photoreactor at selected times. Samples were analyzed by gas chromatography with a thermal conductivity detector (GC-TCD) on an Agilent Technologies 7890A gas chromatograph furnished with a Supelco Carboxen 1010 Plot column. Injector temperature was set at 150ºC and detector at 250ºC. Nitrogen was used as the carrier gas at 20 mL·min^{-1} (4psi, 0.7 mL·min^{-1} through the column). Oven temperature was kept at 70ºC for 2 min, then ramped up to 120ºC at 10ºC·min^{-1}, the final temperature being kept for 13 min.

No activity (i.e. hydrogen production) was observed from suspensions in water of the catalysts submitted to the reaction conditions, thus confirming that hydrogen came from glycerol photoreforming.

3.Results and discussion

3.1. Chemical analysis and morphology

Composition of the samples was firstly studied by X-ray fluorescence analyses. Pure titania solids showed a titanium content in the range 57.1-57.6 wt % which expressed as TiO_2 means 95.3-96.1% of total weight. Moreover, magnesium content of olive leaves is ca. 0.2% whereas this metal is hardly detected in our solids. This confirms the effective

exchange of magnesium by titanium and/or copper during the first step of the synthetic procedure. As regards the copper content, higher values were obtained for Et as compared to IP series. Therefore, copper contents of 0.6-21.0 wt% were obtained for IP series whereas the values in Et series were in the 35.2-45.9 wt% range. If results are expressed as $Cu/(Ti+Cu)$ mol % for all solids, the values are in the 0.8-44.5% range for IP series and between 38.5 and 62.1% for Et series (Table 1, 4th column). These results suggest that copper is more easily incorporated through copper acetate hydrolysis than by cationic exchange with magnesium, despite the fact that Mg^{2+} has a more similar size to Cu^{2+} than to Ti^{3+} (atomic radii of 72, 73 and 67 pm, respectively) [18]. One could argue that even though atomic mass of copper and titanium is relatively high, thus presenting a better X-ray penetration, XRF has a penetration of micrometers and thus copper atoms present in the core of the particles could not be reached. Therefore, in order to have a more accurate determination of bulk composition of samples, they were analyzed by ICP-MS, results been included in Table 1, 5th column. As can be seen, ICP-MS results are quite similar to those found by XRF confirming the higher copper incorporation in Et series as compared to IP one.

Surface composition of samples as determined by XPS is given in Table 1, 6th column. There are 6 catalysts with a $Cu/(Ti+Cu)$ mol % in the 15.6-23.4% range whereas only two catalysts belonging to IP series (CuTi(1:1)|Ti-IP and CuTi(1:3)|Ti-IP) exhibit a significantly lower value (5.8 and 1.9%, respectively). In any case, variation of surface composition of samples is lower than that found for bulk content.

SEM images of two representative solids with and without copper (Ti|Ti-IP and CuTi(1:3)|Ti-IP, respectively) are shown in Figure 1. Moreover, the images of all catalysts are given as supplementary material (Figures S2 and S3). SEM results corroborate the successful replication of olive leaves structure with the trichomes (scaly umbrella-shaped

hair whose function is to prevent water evaporation) and the internal channels (see Figure 1 as an example). Furthermore, elemental mapping (SEM-EDX) of samples evidenced a good dispersion of copper and titanium. Finally, backscattered electrons images of trichomes for Et series are brighter than those of IP solids (see Figures S2 and S3), which is consistent with the copper content as determined by XRF or ICP-MS. Therefore, copper atoms with an atomic weight of 63.54 a.m.u. appears brighter than titanium whose atomic weight is 47.87 a.m.u.

3.2. Textural and structural characterization

N_2 adsorption-desorption isotherms of the samples (Figure S4) are type IV associated to mesoporous materials. BET surface areas and average pore diameters in the 25-75 $m^2 \cdot g^{-1}$ and 3.8-12.4 nm range, respectively, were obtained (Table 1, 2nd and 3rd columns). No clear trend was observed regarding evolution of such parameters with the Cu/Ti ratio.

X-ray diffractograms of all solids are shown in Figure 2. In all cases, titania is only present in the anatase form, with signals in pure TiO_2 solids at 2θ values of 25.36º, 37.84º, 48.02º, 54.00º, 54.13º, 62.72º, 68.89º, 70.13º and 75.13º, associated, respectively, to (101), (004), (200), (105), (211), (213), (116), (220) and (107) reflections (JCPDS No. 86-1156) [19]. In all cases anatase crystallite size, as determined by Scherrer equation, is in the 16-21 nm range (Table 1, 7th column). In the case of the copper-containing solids, the systems with high copper contents (over 17 Cu/(Ti+Cu) mol % as determined by ICP-MS) exhibit CuO monoclinic peaks at 2θ values of 35.31º and 38.49º, assigned to (-111) and (111) reflections, respectively (JCPDS No. 01-071-1166) [20]. CuO crystallite sizes are between 48 and 72 nm (Table 1, 8th column).

Ionic radius of Cu^{2+} in octahedral coordination is larger than that of Ti^{4+} (73 and 60.5 pm, respectively). Therefore, introduction of Cu into anatase structure would result in a

change in lattice parameters [18]. In our case, no clear distortion of anatase lattice parameters was observed in the presence of copper, with values close to a=b=3.789 Å and c=9.508 Å and cell volumes in the 136.5-137.2 Å^3 range in all cases. Similarly, lattice parameters for CuO crystals were ca. a=4.69 Å, b=3.43 Å and c=5.13 Å, with cell volumes between 81.3 and 81.5 Å^3. Furthermore, for the solids with a high copper content, the percentage of CuO monoclinic phase, as determined by XRD, is quite close to the copper content measured by XRF or ICP-MS (compare columns 4, 5 and 8 in Table 1) which is supportive of the separate crystallization of both anatase TiO_2 and monoclinic CuO. Nevertheless, in order to cast further light on the possibility of some copper doping in titania structure, complementary Raman studies were performed since this is known to be a more structure-sensitive technique than XRD [21]. Raman spectra of the solids are depicted in Figure 3. Pure TiO_2 materials exhibit signals at ca. 397, 518 and 640cm^{-1}, which correspond to B_{1g}, A_{1g} and E_g anatase vibration modes, respectively. In the case of the samples with the highest copper contents, a broad band at ca. 270-280 cm^{-1} assigned to A_g mode in monoclinic CuO can be seen as well [22]. It is also possible that B_{2g} mode of CuO, which appears at ca. 620 cm^{-1} [23] overlaps with Eg mode in anatase, which would explain the shift in the band at 640 cm^{-1} to lower wavenumbers in Et series with the introduction of copper. It is also interesting to note the shift and broadening in titania A_{1g} band to lower wavenumbers in Et series for copper-containing solids, which could be indicative of the introduction of some copper into titania structure [24]. Partial substitution of Ti^{4+} by Cu^{2+} would result in oxygen vacancies.

The solids were also analyzed by XPS. Ti2p and Cu2p regions are shown in Figure 4. Bare TiO_2 solids exhibit a main signal at ca. 459.1-459.2 eV which is indicative of Ti^{4+} [25]. In the case of Ti|Ti-Et, there is a shoulder at ca. 458.3 eV which could suggest a higher percentage of Ti^{3+} in this sample. The introduction of copper results in a shift of Ti2p$_{3/2}$

signal to lower binding energies which is attributed in the literature to the formation of Ti^{3+} and oxygen vacancies on TiO_2 [20]. Regarding Cu2p signals, XPS studies of TiO_2-CuO samples should be treated with caution, especially at low CuO loadings, since samples are susceptible to in-situ copper reduction [26]. In our case, CuTi(1:3)|Ti-IP and CuTi(1:1)|Ti-IP solids, with surface copper contents below 6% (Cu/(Ti+Cu)mol%), exhibited $Cu2p_{3/2}$ signals at 932.1 and 933.3 eV, respectively, whereas for higher loadings, $Cu2p_{3/2}$ signal was shifted to higher binding energies (934.5-934.6 eV). Such signals are indicative of Cu^{2+}, confirmed by the satellite peaks due to ligand to metal charge transfer, which would be absent in Cu^+ and Cu^0 [27,28]. The upshift of Cu^{2+} signals together with the low-shift of Ti^{4+} peaks has been suggested as indicative of a strong interaction of CuO and TiO_2 [28]. Finally, UV-Vis spectra of the solids were recorded. The corresponding band-gap values collected in Table 1 (9th column), were calculated from the plot of the modified Kubelka-Munk equation as a function of the absorbed light energy (Figure 5). Ti-IP and Ti-Et have band gap values of 2.78 and 2.91 eV, respectively. These values are slightly below those described for anatase and as previously reported could be associated to the presence of structural defects (such as oxygen vacancies) [9]. Moreover, as expected, the introduction of copper resulted in a reduction of the band gap energy [26,29].

3.3. Photocatalytic performance

The solids were tested for hydrogen production through glycerol photoreforming. The main results under UV-radiation are shown in Figure 6A and 6B. As far as the bare TiO_2 solids are concerned, hydrogen production is greater with Ti|Ti-Et than with Ti|Ti-IP (0.76 and 0.26 mmol $H_2 \cdot g_{cat}^{-1}$, respectively, after 6h under UV light). The presence of more defects in the former solid, as evidenced by XPS, could account for that. Furthermore, in all cases TiO_2-CuO solids exhibit a better catalytic performance than pure TiO_2 solids. Focusing on

12

IP series, there is a gradual increase in H_2 production with copper content until CuTi(3:1)|Ti-IP solid which led to 21.9 mmol $H_2 \cdot g_{cat}^{-1}$ after 6h under UV light. Subsequent increase in the copper content resulted in a drop in catalytic performance (9.7 mmol $H_2 \cdot g_{cat}^{-1}$ at t=6h for Cu|Ti-IP). In the case of Et series, Ti|CuTi(1:3)-Et, Ti|CuTi(1:1)-Et and Ti|CuTi(3:1)-Et exhibited quite a similar catalytic performance (17.8-18.7 mmol $H_2 \cdot g_{cat}^{-1}$ for t=6h), a bit lower than that achieved by CuTi/3:1)|Ti-IP. Similarly to IP series, subsequent increase in copper content resulted in a drop in catalytic activity (11.3 mmol $H_2 \cdot g_{cat}^{-1}$ after 6h for Ti|Cu-Et).

The synergistic effect of TiO_2-CuO composites for hydrogen production is usually attributed to a p-n heterojunction between CuO and TiO_2. There is an electron transfer from TiO_2 to CuO, which has a conduction band edge lower than that of TiO_2 (Figure 7A). Therefore, on illumination, electrons accumulate at the CuO conduction band whose potential is below zero and can thus reduce H^+ to H_2. Meanwhile, holes accumulated at the valence band of TiO_2 and CuO are used to oxidize sacrificial agent (glycerol) [22,26,30]. There are, however, many different factors influencing photocatalytic activity such as TiO_2 particle size and crystal structure, CuO content, CuO crystallinity and band-gap energy, among others [28,31,32]. This makes interpretation of results difficult, though one can try to look for the most influential parameters under our experimental conditions. In our case, titania has similar crystallite sizes and consists in 100% anatase particles. Looking at the trend in photocatalytic activity and characterization data summarized in Table 1, there is a certain relationship between surface copper content, as determined by XPS, and hydrogen production. Such a relationship is illustrated in Figure 7B. Therefore, within IP series H_2 production progressively increases in parallel to copper content until a Cu/(Ti+Cu) mol % of 17.8. Subsequent increase in the ratio up to 23.4% results in a drop in H_2 yield. In the case of Et series, the three solids exhibiting similar catalytic performance do also have quite

close surface compositions, with copper contents in the 15.5-17.5% range. Again, Ti|Cu-Et with a greater surficial copper content (20.45%) leads to lower hydrogen yields. According to the literature, there is an optimum CuO content over which photocatalytic activity drops. As explained above, TiO_2-CuO heterojunction is very effective in separating the photogenerated charge carriers and thus enhancing the photocatalytic activity. Nevertheless, an excessive CuO content results in the increase in charge carriers recombination effect and the increase in the opacity of the suspension (shielding effect) which is detrimental to the activity [31,33]. In our case, the optimum CuO content seems to be close to Cu/(Ti+Cu) mol % of 17. The fact that CuTi(3:1)|Ti-IP and Ti|CuTi(3:1)-Et with Cu/(Ti+Cu) mol % of 17.8 and 17.6, respectively, differs a 23% in activity suggest the influence of some other features such as the band gap value or the CuO particle size. In fact, band-gap values of those solids are 1.88 and 2.36 eV, respectively. Nevertheless, under UV irradiation that difference should not be so important since the energy of photons is high enough as to promote electrons from the valence to the conduction band in both cases. As for CuO particle size, monoclinic CuO crystals are hardly seen in CuTi(3:1)|Ti-IP solid whereas they are clearly evident in Ti|CuTi(3:1)-Et solid. This suggests greater crystallites in the latter case. As CuO crystallite size increases, CuO conduction band becomes more positive with respect to H^+/H_2 couple which eventually prevent direct transfer of electrons from CuO to H^+ and thus H_2 formation [26]. All in all, in the best of the cases (Cu|Ti(3:1)Ti-IP solid), hydrogen photoproduction achieved is 84 times higher than that obtained on bare titania, under UV irradiation. Therefore, 21.9 mmol H_2 g_{cat}^{-1} were obtained after 6h (ca. 3.7 mmol $H_2 \cdot g_{cat}^{-1} \cdot h^{-1}$).

Hydrogen production values obtained after 24h of irradiation under solar-simulated light are shown in Figure 6C and 6D. Similarly to reactions under UV light, the presence of copper in the solids leads to an improvement in catalytic activity up to a value over which

higher copper contents are detrimental to activity. Moreover, the effect on the synthetic method (Et or IP series) seems to be clearer than under UV light, the solids belonging to IP series exhibiting a better catalytic performance. It is important to note that TiO_2 only absorbs ca. 5% of solar light. Therefore, the role of copper under solar light according to the mechanism illustrated in Figure 7A is more significant than for UV light in which case a much greater amount of incident light is absorbed by TiO_2. Figure S5 compares TPR profiles of CuTi(3:1)|Ti-IP and Ti|CuTi(1:3)-Et solids (the most active catalyst under visible light within IP and Et series, respectively). The area under the curves is dependent on the copper content, thus accounting for Ti|CuTi(1:3)-Et TPR area being ca. 2.5 times higher that of CuTi(3:1)|Ti-IP (compare copper contents in table 1, 5th column). Furthermore, TPR peaks in CuTi(3:1)|Ti-IP are shifted to lower temperatures thus indicating its better reducibility which, in turn, could be associated to the lower CuO particle size for IP series (remember XRD results, table 1 8th column). This better reducibility of copper in IP series would explain the higher hydrogen production values under solar-simulated light. All in all, similarly as for experiments under UV light, Cu|Ti(3:1)Ti-IP solid exhibited again the highest hydrogen production under solar light, 13.7 mmol $H_2 \cdot g_{cat}^{-1}$ after 24h (ca. 0.57 mmol $H_2 \cdot g_{cat}^{-1} \cdot h^{-1}$). Finally, results obtained for a physical mixture of Ti|Ti-IP and commercial CuO under UV and solar-simulated irradiation are shown in Figures 6B and 6D, respectively. As can be seen, though the solids exhibited a better catalytic performance than Ti|Ti-IP as a result of the possibility of electron transfer from TiO_2 to CuO [15], hydrogen production is lower than for the most active solids within Et and IP series where the contact between both oxides is more intimate.

4.Conclusions

Olive leaf structure was successfully replicated in several TiO_2-CuO solids. Incorporation of copper through chemical exchange with magnesium (II) in porphyrin rings was lower than that resulting from hydrolysis of copper (II) acetate in ethanol medium. In all cases TiO_2 crystallized in the anatase form only. In the case of copper-containing solids, no crystal phases were detected for copper contents below 15wt% whereas for larger percentages monoclinic CuO was seen by XRD and Raman. XPS revealed the existence of a TiO_2-CuO interaction as evidenced by the shift of the Ti^{4+} 2p and Cu^{2+} 2p signals to lower and higher binding energies values, respectively. Furthermore, incorporation of copper resulted in a decrease in the band gap value. The solids were tested for hydrogen production through glycerol photoreforming, catalytic activity increasing on copper introduction as a result of the p-n heterojunction. Moreover, UV experiments showed that there is an optimum surface Cu/ (Ti+Cu) mol %, close to 17%, above which further increase resulted in a decrease in catalytic performance. It is possible that an excessive copper content promotes electron-hole recombination and the shielding effect by CuO particles prevents light absorption by titania particles. In the best case, catalytic activity of bare titania was multiplied by 84 under UV-light (ca. 3.65 mmol $H_2 \cdot g_{cat}^{-1} \cdot h^{-1}$ achieved on CuTi(3:1)|Ti-IP). Results found under solar-simulated light are better for IP than for Et series. TPR results evidenced a higher reducibility of CuO particles in IP series as compared to Et, which, in turn, could be associated to the lower CuO crystallite size. All in all, similarly as for UV series, the most active solid was CuTi(3:1)|Ti-IP producing ca. 0.57 mmol $H_2 \cdot g_{cat}^{-1} \cdot h^{-1}$.

Acknowledgements

References

[1]   H. Zhou, T. Fan, D. Zhang, ChemSusChem 4 (2011) 1344–1387.

[2]   K. Liu, L. Jiang, in: R. Xu, W. Pang, Q. Huo (Eds.), Mod. Inorg. Synth. Chem., 2011, pp. 525–553.

[3]   A. Cai, X. Wang, Y. Qi, Z. Ma, Appl. Surf. Sci. 391 (2017) 484–490.

[4]   E. Shimoni, O. Rav-Hon, I. Ohad, V. Brumfeld, Z. Reich, Plant Cell 17 (2005) 2580–2586.

[5]   H. Zhou, X. Li, T. Fan, F.E. Osterloh, J. Ding, E.M. Sabio, D. Zhang, Q. Guo, Adv. Mater. 22 (2010) 951–956.

[6]   C.S. Sathu, Naveen K; Devaraji, Perumal; Gopinath, J. Nanosci. Nanotechnol. 16 (n.d.) 9203–9208.

[7]   I. Hashemizadeh, V.B. Golovko, J. Choi, D.C.W. Tsang, A.C.K. Yip, Chem. Eng. J. 347 (2018) 64–73.

[8]   I. Tseng, L. Kang, P. Chang, M. Tsai, J. Yeh, T. Yang, 4 (2019) 1636–1644.

[9]   J. Hidalgo-Carrillo, J. Martín-Gómez, M.C. Herrera-Beurnio, R.C. Estévez, F.J. Urbano, A. Marinas, Nanomaterials 10 (2020) 1057.

[10]   E. Saeb, K. Asadpour-zeynali, Microchem. J. 160 (2020) 105603.

[11]   H. Shu, M. Yang, Q. Liu, M. Luo, Coatings 10 (2020) 179.

[12]   L. Cheng, S. Qiu, J. Chen, J. Shao, S. Cao, Mater. Chem. Phys. 190 (2017) 53–61.

[13]   S. ichiro Fujita, H. Kawamori, D. Honda, H. Yoshida, M. Arai, Appl. Catal. B Environ. 181 (2016) 818–824.

[14] M.G. Méndez-Medrano, E. Kowalska, B. Ohtani, D. Bahena Uribe, C. Colbeau-Justin, S. Rau, J.L. Rodríguez-López, H. Remita, J. Chem. Phys. 153 (2020) 034705.

[15] J. Hidalgo-Carrillo, V. Montes, J. Martín-Gómez, R.C. Estévez-Toledano, J.C. Escamilla, A. Marinas, F.J. Urbano, J. Environ. Chem. Eng. 9 (2021) 105336.

[16] M.C. Ortega-Liébana, E. Sánchez-López, J. Hidalgo-Carrillo, A. Marinas, J.M. Marinas, F.J. Urbano, Appl. Catal. B Environ. 127 (2012) 316–322.

[17] C.G. Hatchard, C.A. Parker, Proc. R. Scociets London. Ser. A, Math. Phys. Sci. 235 (1956) 518–536.

[18] R.D. Shannon, Acta Cryst. A 32 (1976) 751–767.

[19] S.F. Shaikh, R.S. Mane, B.K. Min, Y.J. Hwang, O.S. Joo, Sci. Rep. 6 (2016) 1–10.

[20] A.F. Zedan, N.K. Allam, S.Y. Alqaradawi, Catalysts 7 (2017) 129.

[21] A.M. Alotaibi, B.A.D. Williamson, S. Sathasivam, A. Kafizas, M. Alqahtani, C. Sotelo-Vazquez, J. Buckeridge, J. Wu, S.P. Nair, D.O. Scanlon, I.P. Parkin, ACS Appl. Mater. Interfaces 12 (2020) 15348–15361.

[22] M.M. Hasan, N.K. Allam, RSC Adv. 8 (2018) 37219–37228.

[23] S.J.A. Moniz, J. Tang, ChemCatChem 7 (2015) 1659–1667.

[24] J. Navas, A. Sánchez-Coronilla, T. Aguilar, N.C. Hernández, D.M. De Los Santos, J. Sánchez-Márquez, D. Zorrilla, C. Fernández-Lorenzo, R. Alcántara, J. Martín-Calleja, Phys. Chem. Chem. Phys. 16 (2014) 3835–3845.

[25] A.P. Singh, N. Kodan, B.R. Mehta, Appl. Surf. Sci. 372 (2016) 63–69.

[26] W.T. Chen, V. Jovic, D. Sun-Waterhouse, H. Idriss, G.I.N. Waterhouse, Int. J. Hydrogen Energy 38 (2013) 15036–15048.

[27] P. Khemthong, P. Photai, N. Grisdanurak, Int. J. Hydrogen Energy 38 (2013) 15992–16001.

[28] S.M. Park, A. Razzaq, Y.H. Park, S. Sorcar, Y. Park, C.A. Grimes, S. Il In, ACS Omega 1 (2016) 868–875.

[29] C. Castañeda, F. Tzompantzi, A. Rodríguez-Rodríguez, M. Sánchez-Dominguez, R. Gómez, J. Chem. Technol. Biotechnol. 93 (2018) 1113–1120.

[30] J. Yu, Y. Hai, M. Jaroniec, J. Colloid Interface Sci. 357 (2011) 223–228.

[31] A. Kubiak, Z. Bielan, M. Kubacka, E. Gabała, A. Zgoła-Grześkowiak, M. Janczarek, M. Zalas, A. Zielińska-Jurek, K. Siwińska-Ciesielczyk, T. Jesionowski, Appl. Surf. Sci. 520 (2020) 146344.

[32] S. Mathew, P. Ganguly, S. Rhatigan, V. Kumaravel, C. Byrne, S.J. Hinder, J. Bartlett, M. Nolan, S.C. Pillai, Appl. Sci. 8 (2018) 2067.

[33] M. Rokhmat, E. Wibowo, Sutisna, Khairurrijal, M. Abdullah, Procedia Eng. 170 (2017) 72–77.

Table 1. Some features concerning characterization of the catalysts synthesized in the present study.

Catalyst	N$_2$ adsorption-desorption isotherms		XRF	ICP-MS	XPS	XRD		UV-Vis
	BET Surface (m^2/g)	Average pore diameter (nm)	Cu/(Ti+Cu) mol%	Cu/(Ti+Cu) mol%	Cu/(Ti+Cu) mol %	TiO$_2$ anatase % (crystallite size in nm)	CuO monoclinic % (crystallite size in nm)	Band gap (eV)
Ti|Ti-IP	31	6.1	0.0	0.0	0.0	100 (19)	0	2.78
CuTi(1:3)|Ti-IP	75	3.8	0.8	1.0	1.9	100 (17)	0	2.75
CuTi(1:1)|Ti-IP	25	6.2	2.5	3.0	5.8	100 (21)	0	2.56
CuTi(3:1)|Ti-IP	29	10.1	14.4	16.6	17.8	100 (16)	0	1.88
Cu|Ti-IP	79	6.5	44.5	40.6	23.4	56 (19)	44 (72)	2.54
Ti|Ti-Et	42	5.5	0.0	0.0	0.0	100 (21)	0	2.91
Ti|CuTi(1:3)-Et	51	9.8	38.5	42.3	15.6	58.5 (18)	41.5 (48)	2.64
Ti|CuTi(1:1)-Et	28	12.4	52.2	55.2	17.4	49.2 (19)	50.8 (71)	2.44
Ti|CuTi(3:1)-Et	53	7.3	54.9	59.7	17.6	46.7 (17)	53.3 (57)	2.36
Ti|Cu-Et	66	6.4	62.1	62.3	20.5	36.6 (17)	63.4 (56)	1.84

Caption to figures

Figure 1. SEM (A) and Backscattered SEM (B) images of Ti|Ti-IP and CuTi(1:3)|Ti-IP. (C) Elemental mapping (SEM-EDX) of the samples indicating the distribution of Cu and Ti.

Figure 2. XRD patterns of the catalysts. The circle and the triangle indicate significant diffraction peaks of anatase TiO_2 and monoclinic CuO, respectively.

Figure 3. Raman spectra of the catalysts. The circle and the triangle indicate distinctive peaks of anatase TiO_2 and monoclinic CuO, respectively.

Figure 4. X-ray photoelectron (XPS) profiles of Ti2p (A) and Cu2p (B) regions.

Figure 5. Calculation of band-gap energy of the catalysts plotting the transformed Kubelka-Munk function vs the energy of the absorbed light. Pictures of the different catalysts are also included.

Figure 6. Hydrogen photoproduction on the different catalysts under UV (A and B) or solar-simulated (C and D.irradiation. Reaction conditions: 5 mL of a 10%v/v glycerol in water solution and 5mg catalyst. Results found for a physical mixture of Ti|Ti-IP and commercial CuO (85:15 w/w) have also been included for the sake of comparison.

Figure 7. A) Illustration of the charge transfer and separation in TiO_2-CuO heterojunctions adapted from [30]. B) Hydrogen production in experiments under UV irradiation as a function of the surface Cu/(Cu+Ti) mol % of the catalysts as determined by XPS.

Figure S1. UV (A and B) and solar-simulated (C and D) equipment used in the present work.

Figure S2. SEM (A) and Backscattered SEM (B) images of the solids belonging to IP series. (C) Elemental mapping (SEM-EDX) of the samples indicating the distribution of Cu and Ti.

Figure S3. SEM (A) and Backscattered SEM (B) images of the solids belonging to Et series. (C) Elemental mapping (SEM-EDX) of the samples indicating the distribution of Cu and Ti.

Figure S4. Nitrogen adsorption-desorption isotherms of the solids synthesized in the present study.

Figure S5. TPR profiles for CuTi(3:1)|Ti-IP and Ti|CuTi (1:3)-Et catalysts.

**Ti|Ti-IP**   **CuTi(1:3)|Ti-IP**

A)

B)

C)

Ti Kα1   Ti Kα1   Ti Kα1   Ti Kα1

Cu Lα1_2   Cu Lα1_2
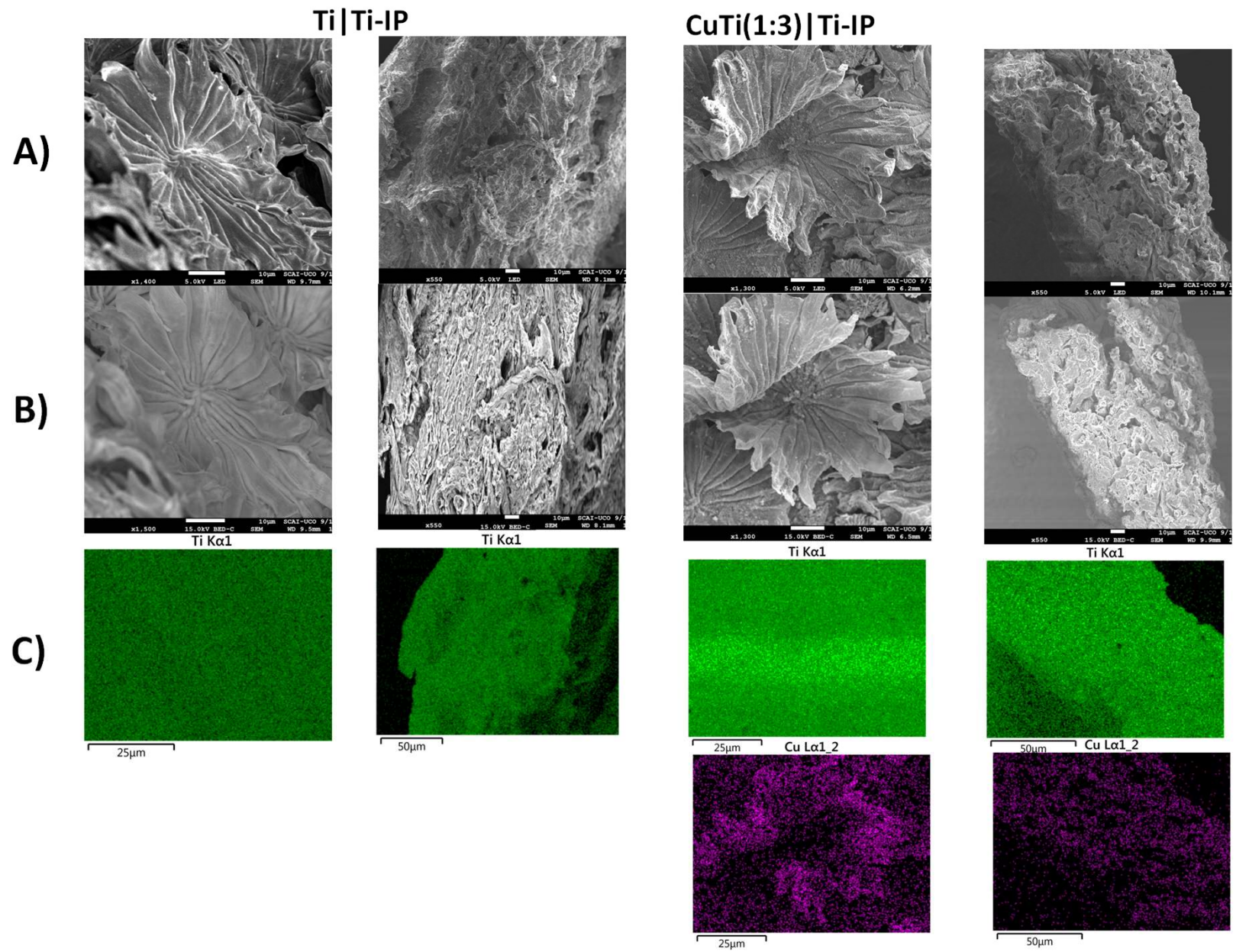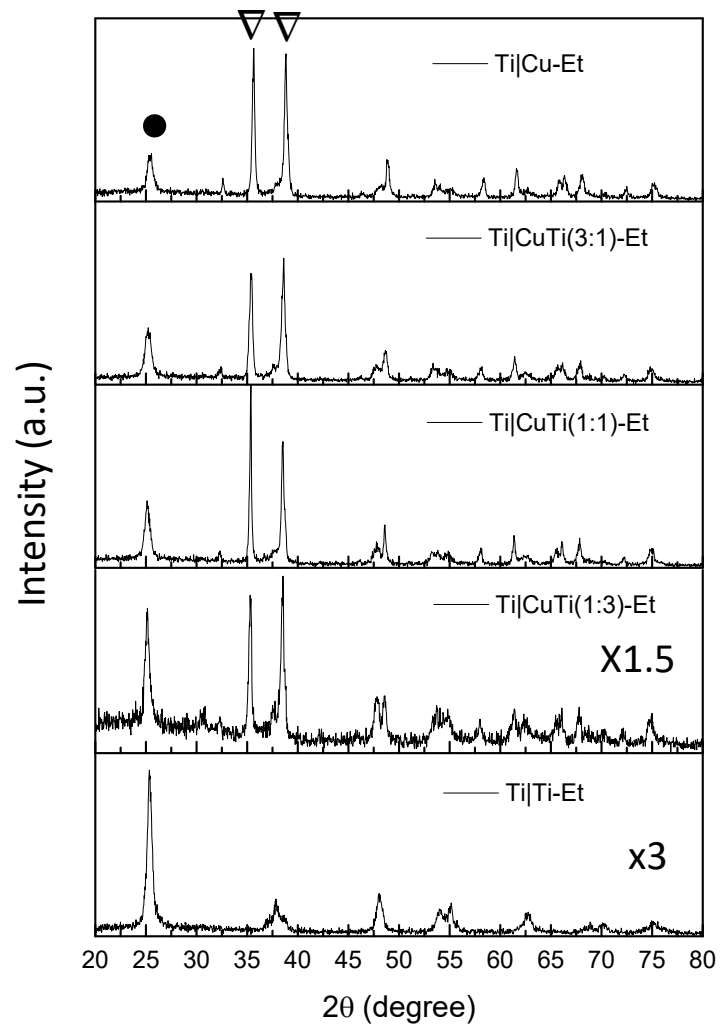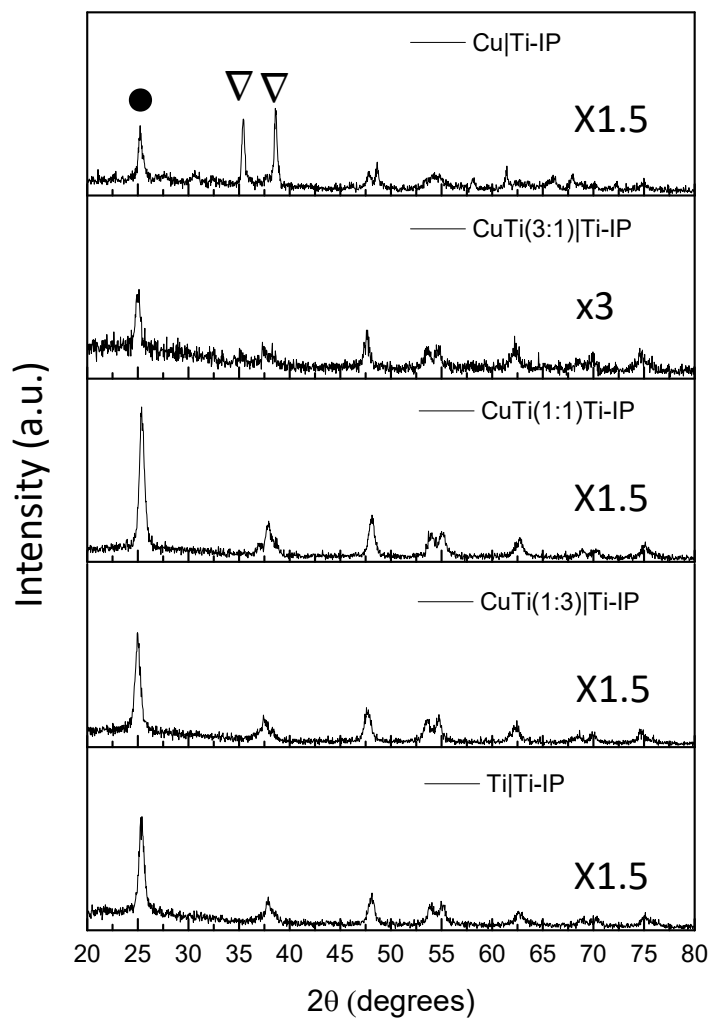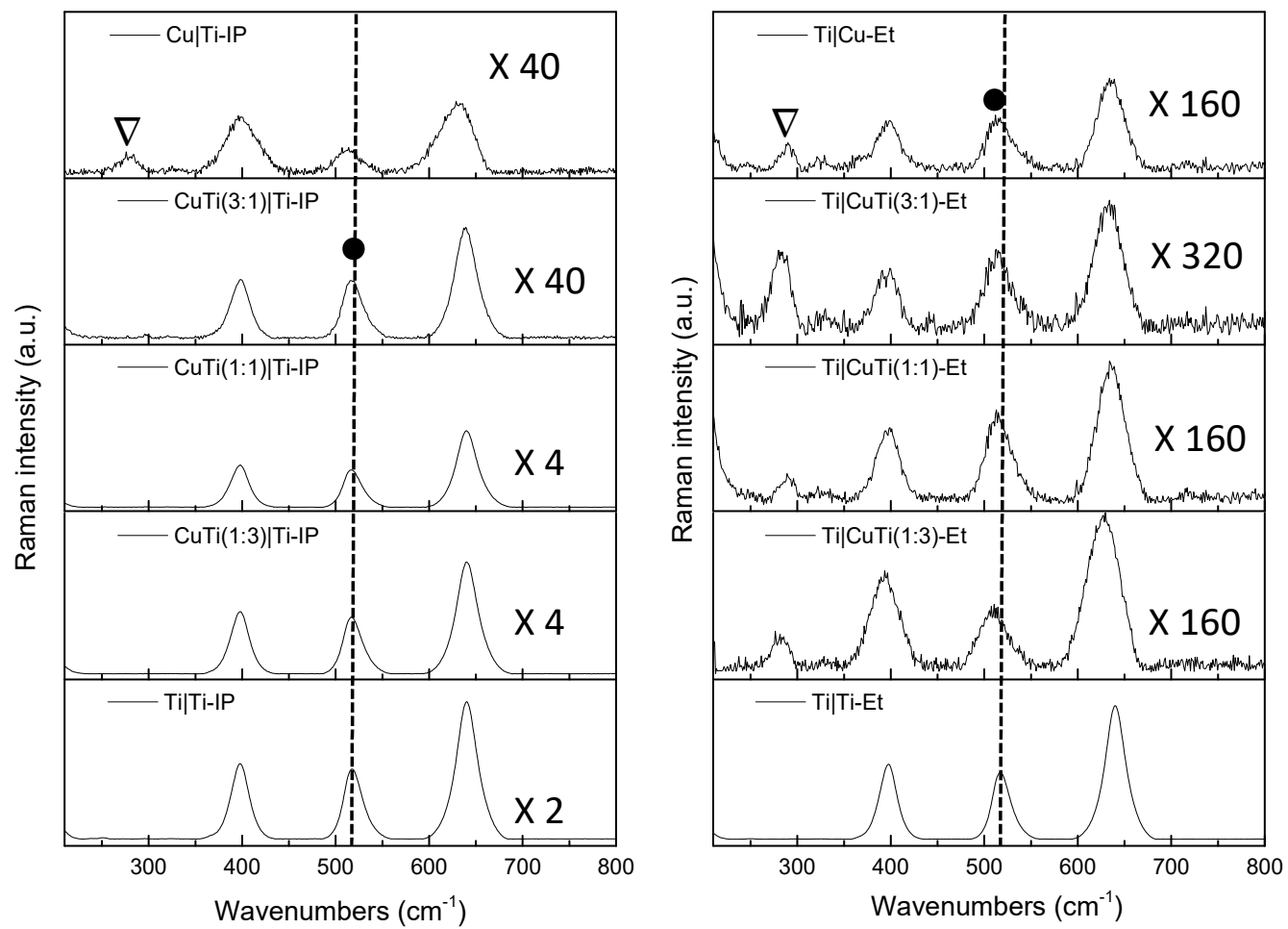
Figure 1.

Figure 2

Figure 3
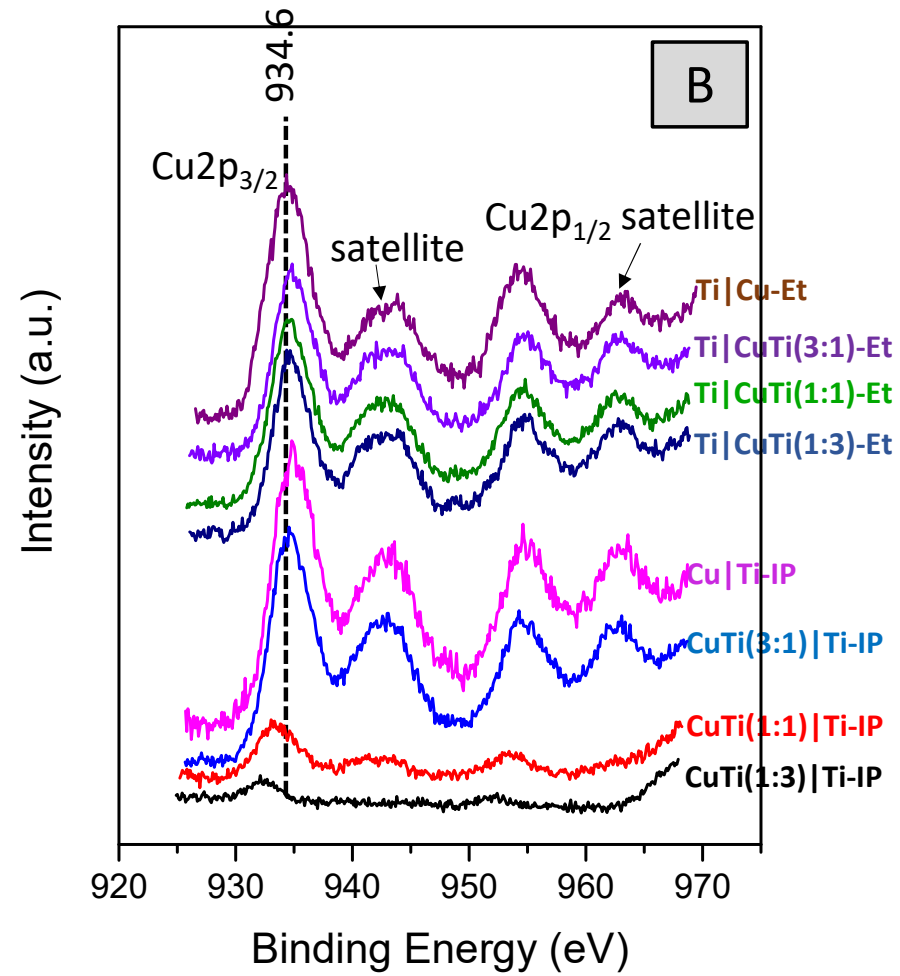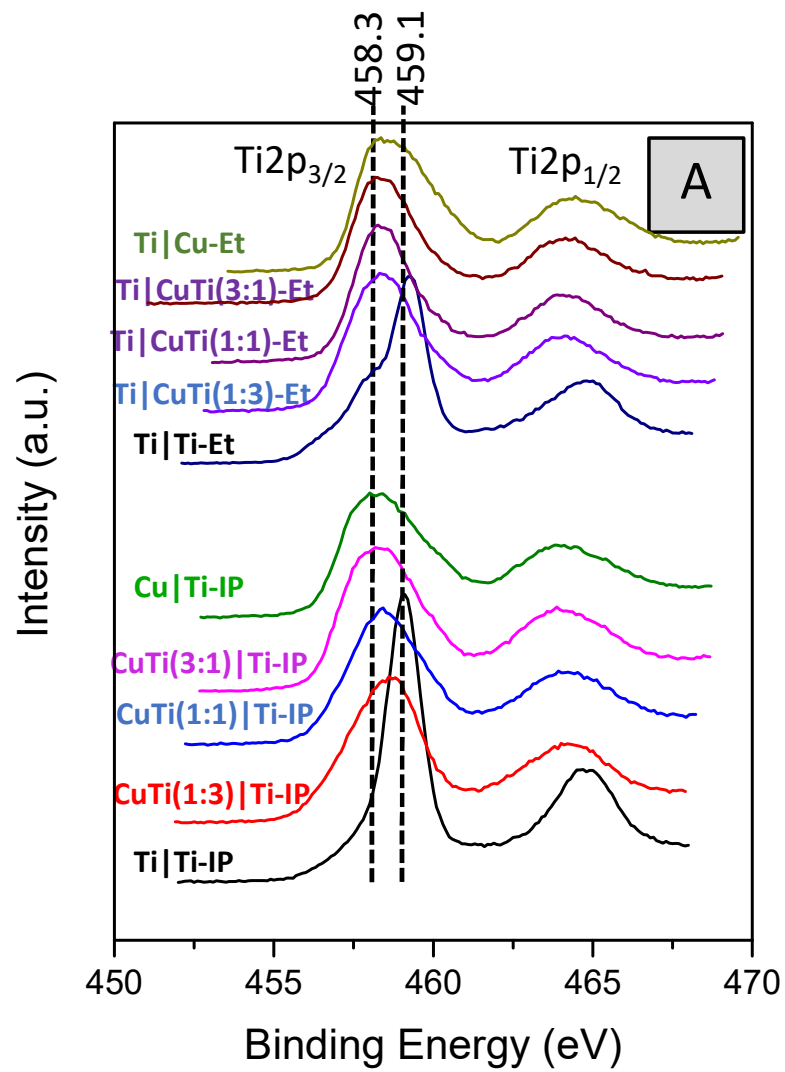
Figure 4
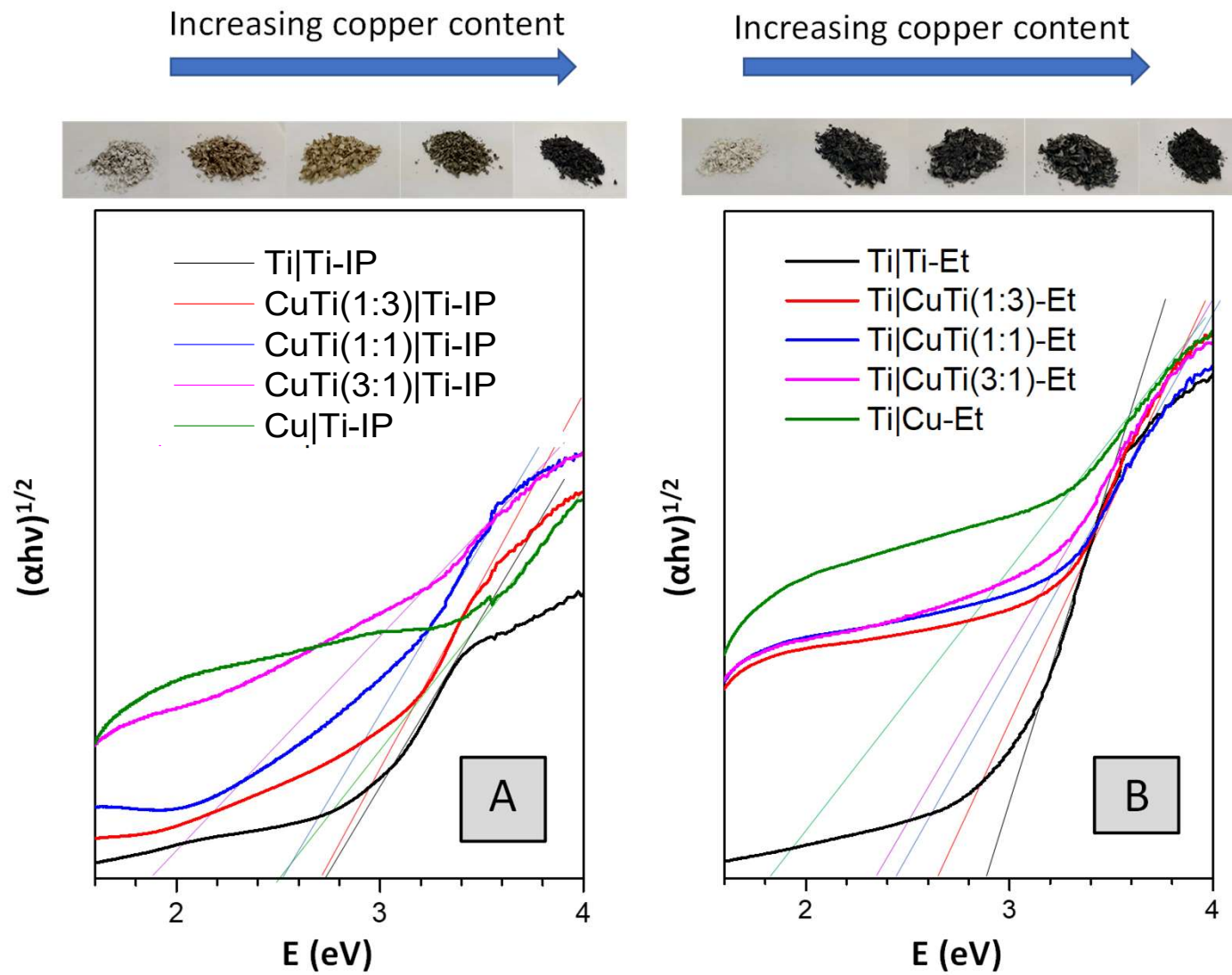
Figure 5
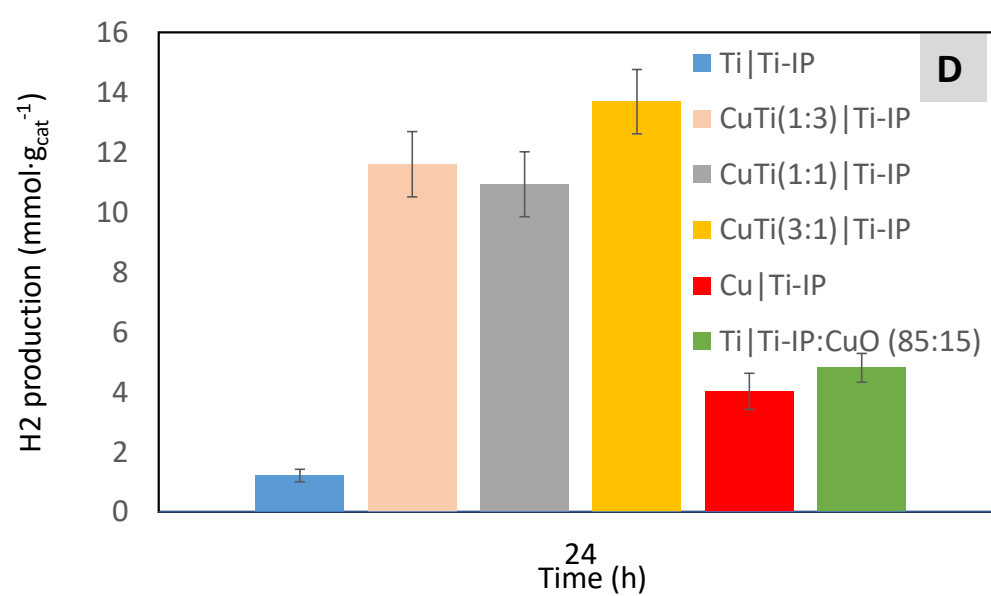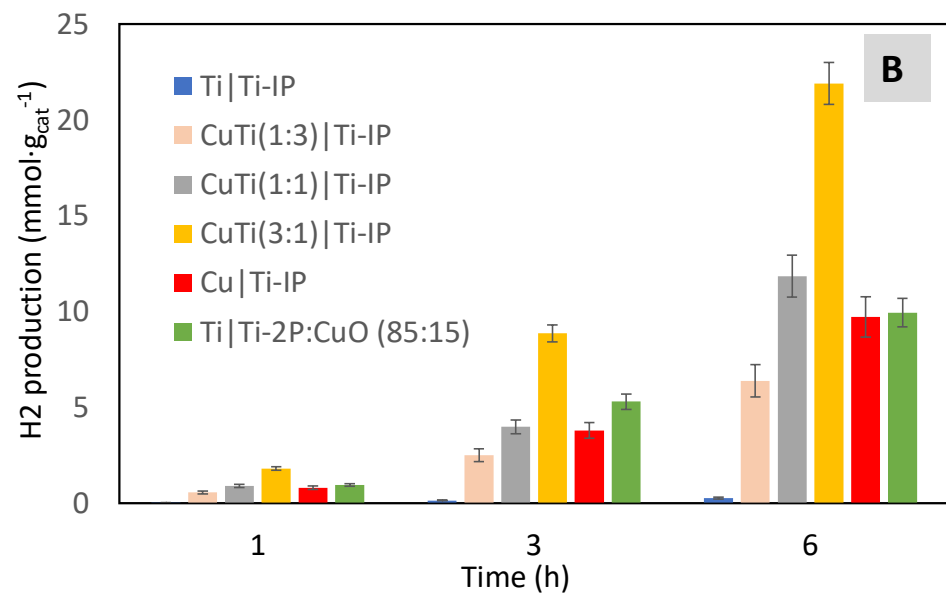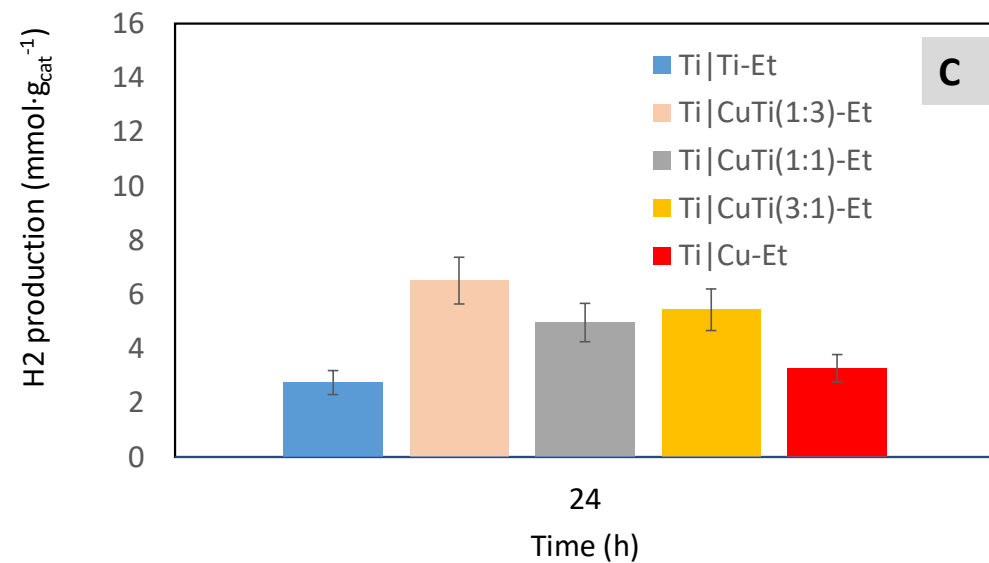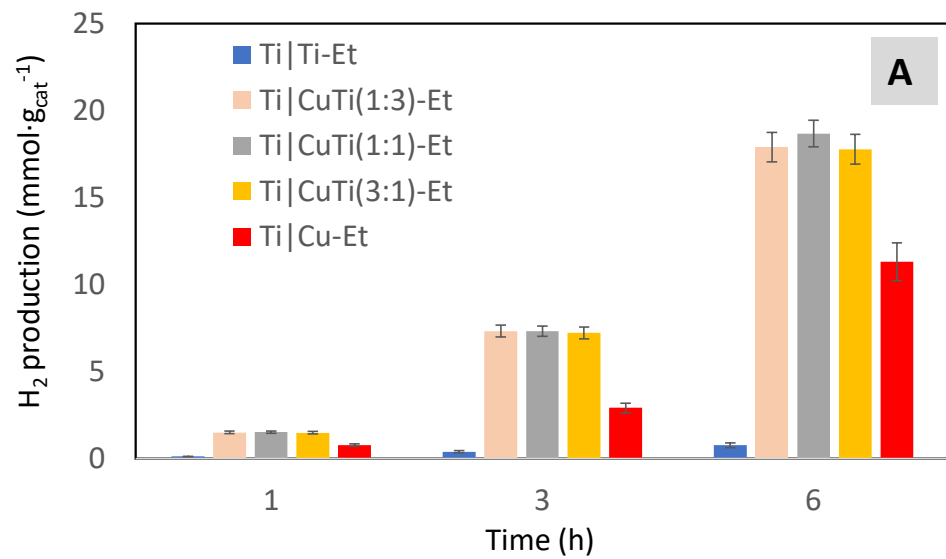
Figure 6

Figure 7

Figure S1.

Ti|Ti-IP   CuTi(1:3)|Ti-IP   CuTi(1:1)|Ti-IP   CuTi(3:1)|Ti-IP   Cu|Ti-IP

Figure S2.

Figure S2 (cont.)

Ti|Ti-Et **Ti|CuTi(1:3)-Et** **Ti|CuTi(1:1)-Et** **Ti|CuTi(3:1)-Et** **Ti|Cu-Et**

A)

B)

C)

Ti Kα1

Cu Lα1_2

Figure S3.

Ti|Ti-Et **Ti|CuTi(1:3)-Et** **Ti|CuTi(1:1)-Et** **Ti|CuTi(3:1)-Et** **Ti|Cu-Et**

A)

B)

C)

Ti Kα1

Cu Lα1_2
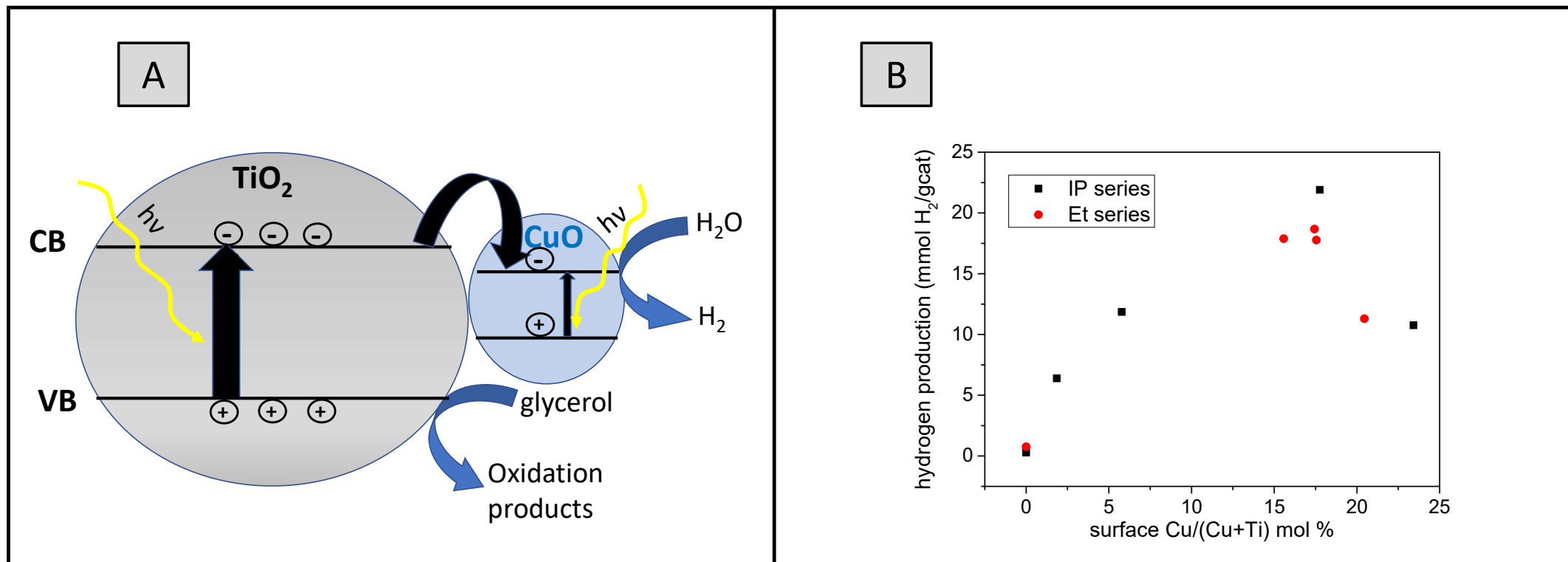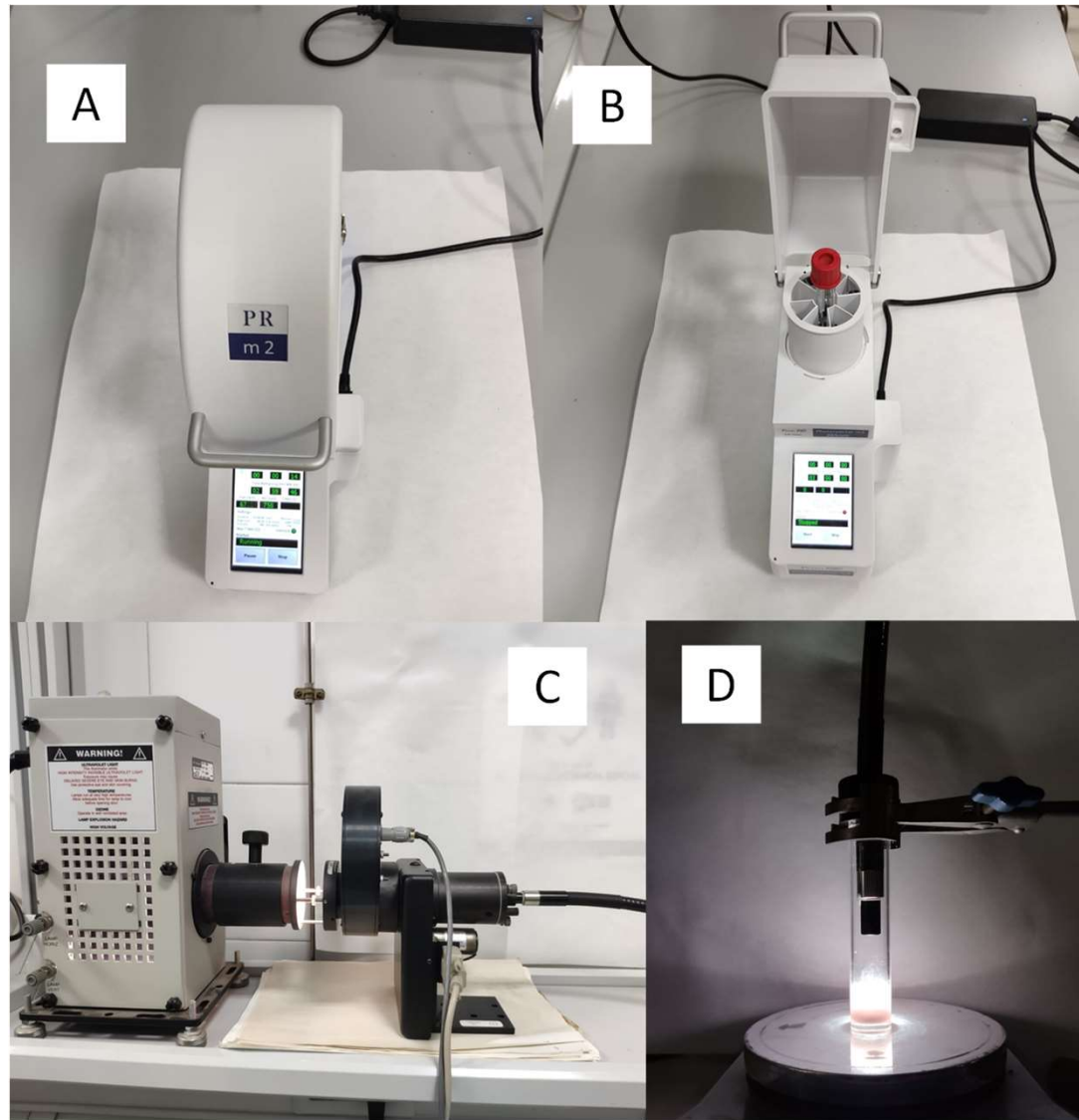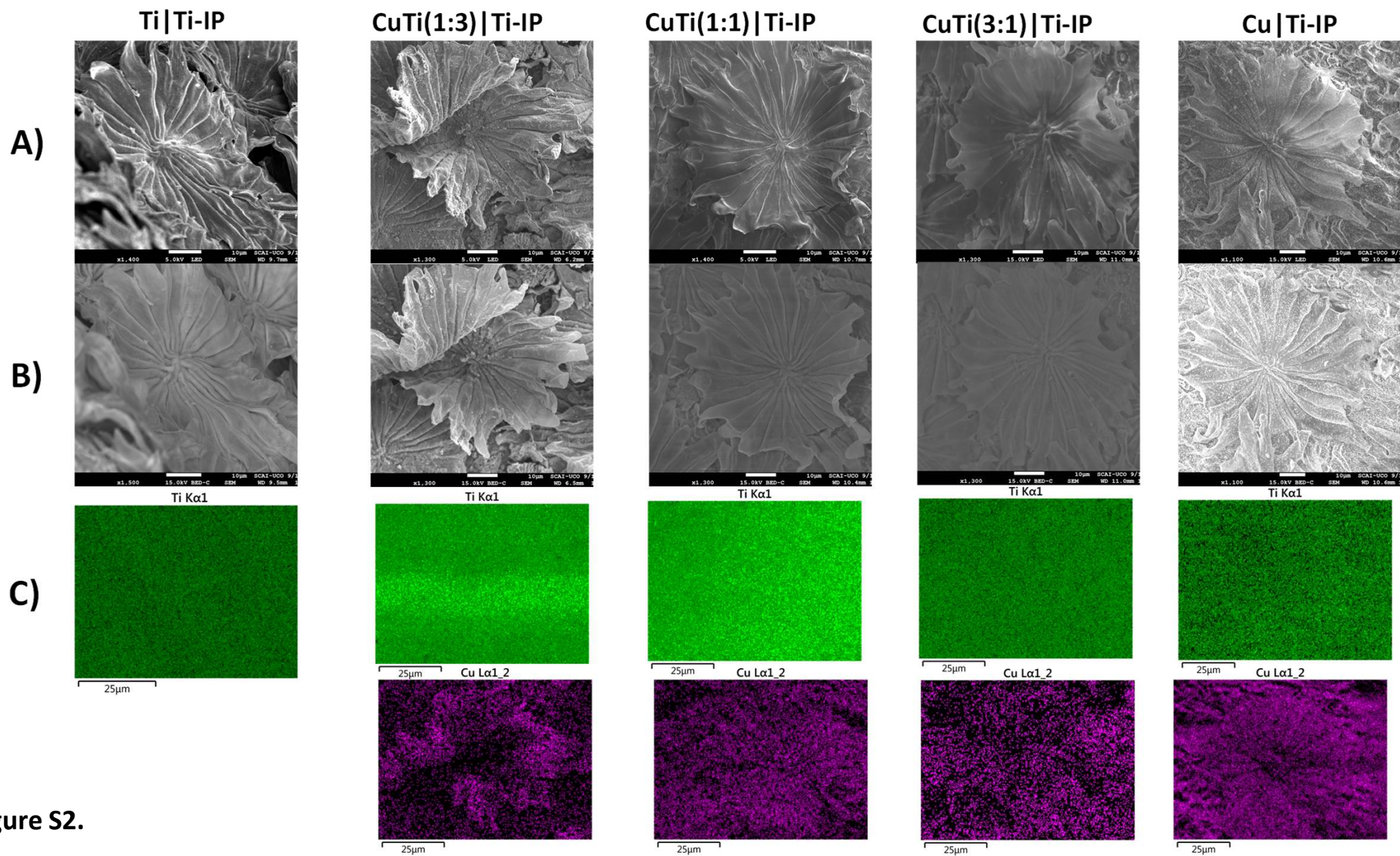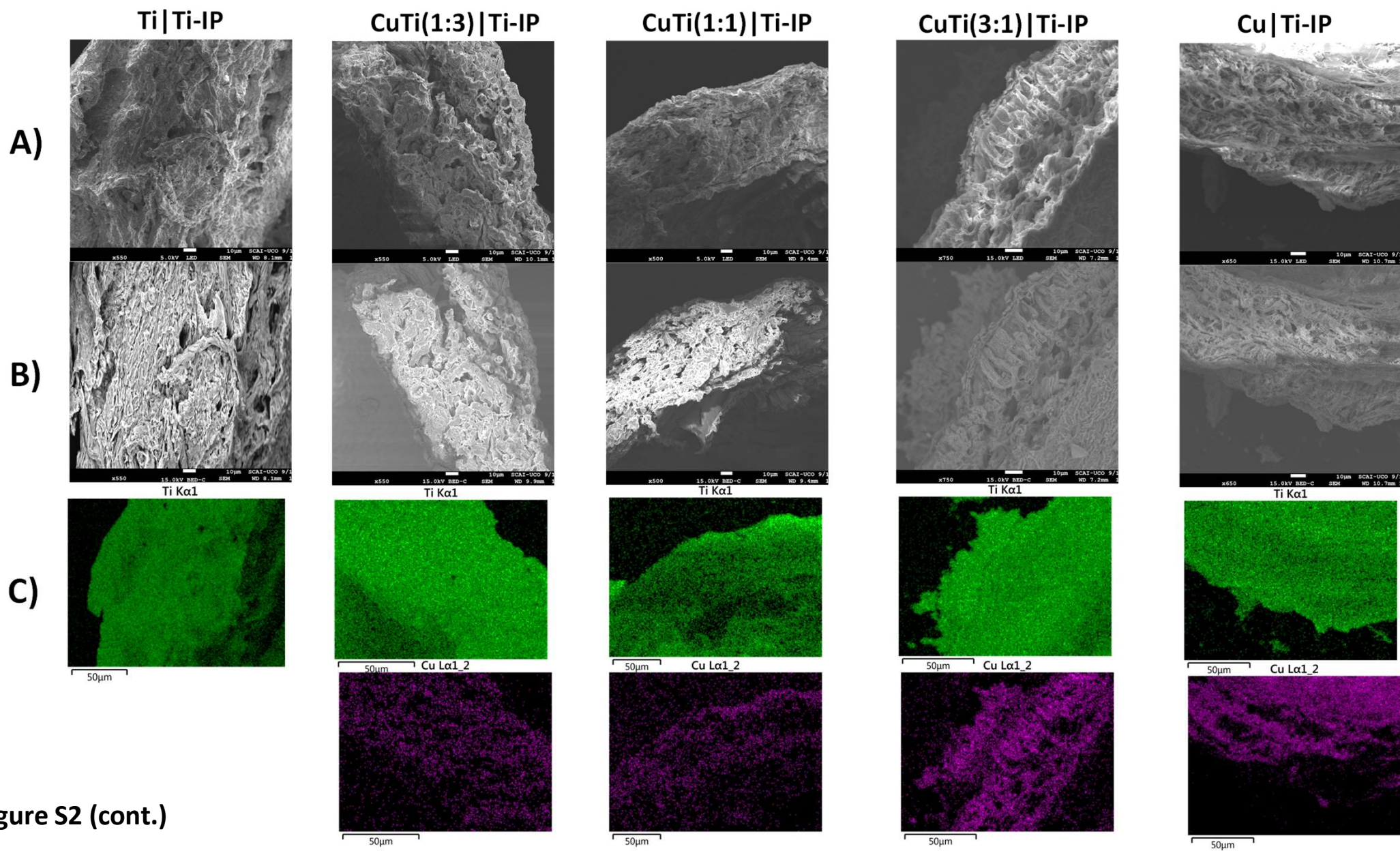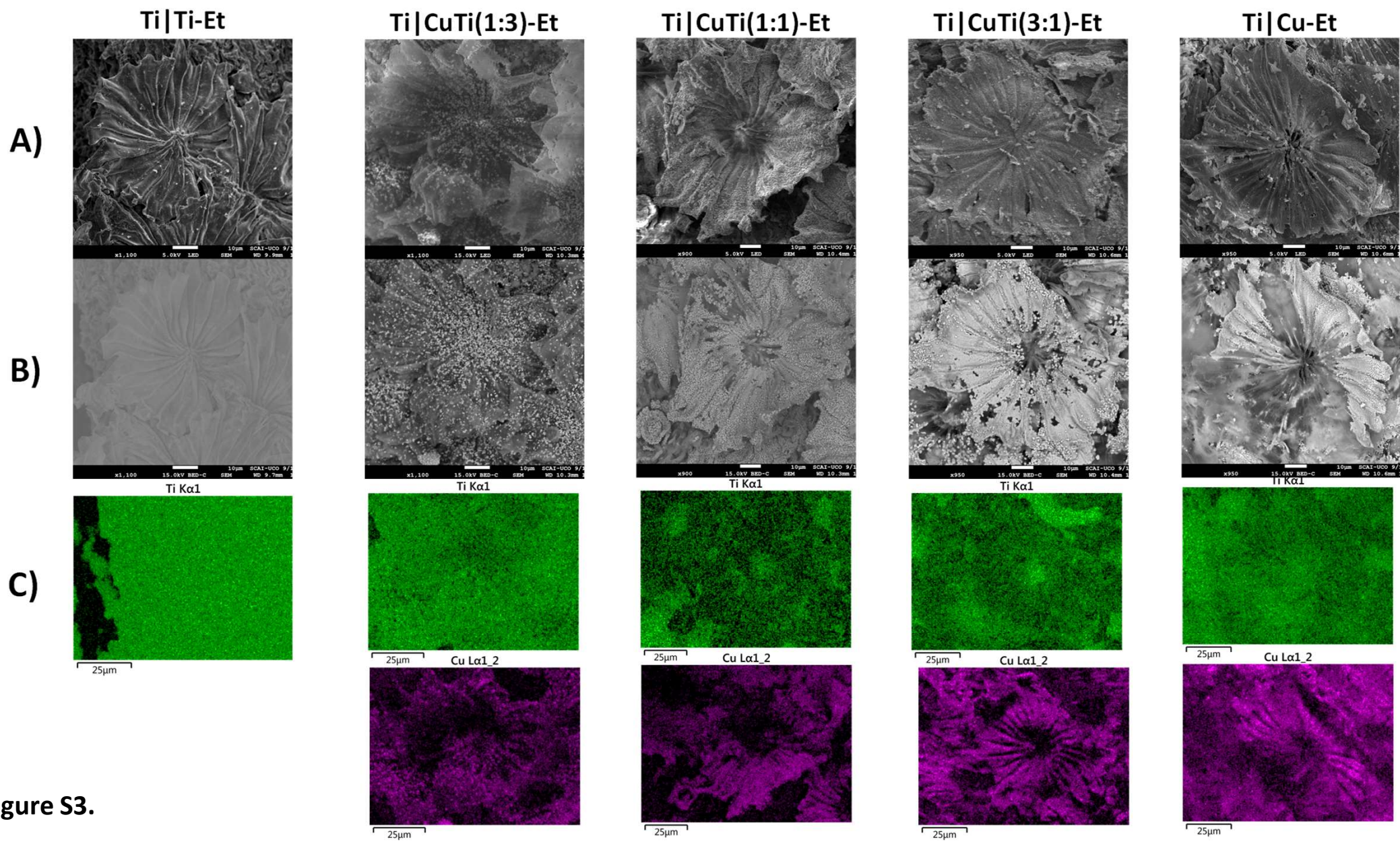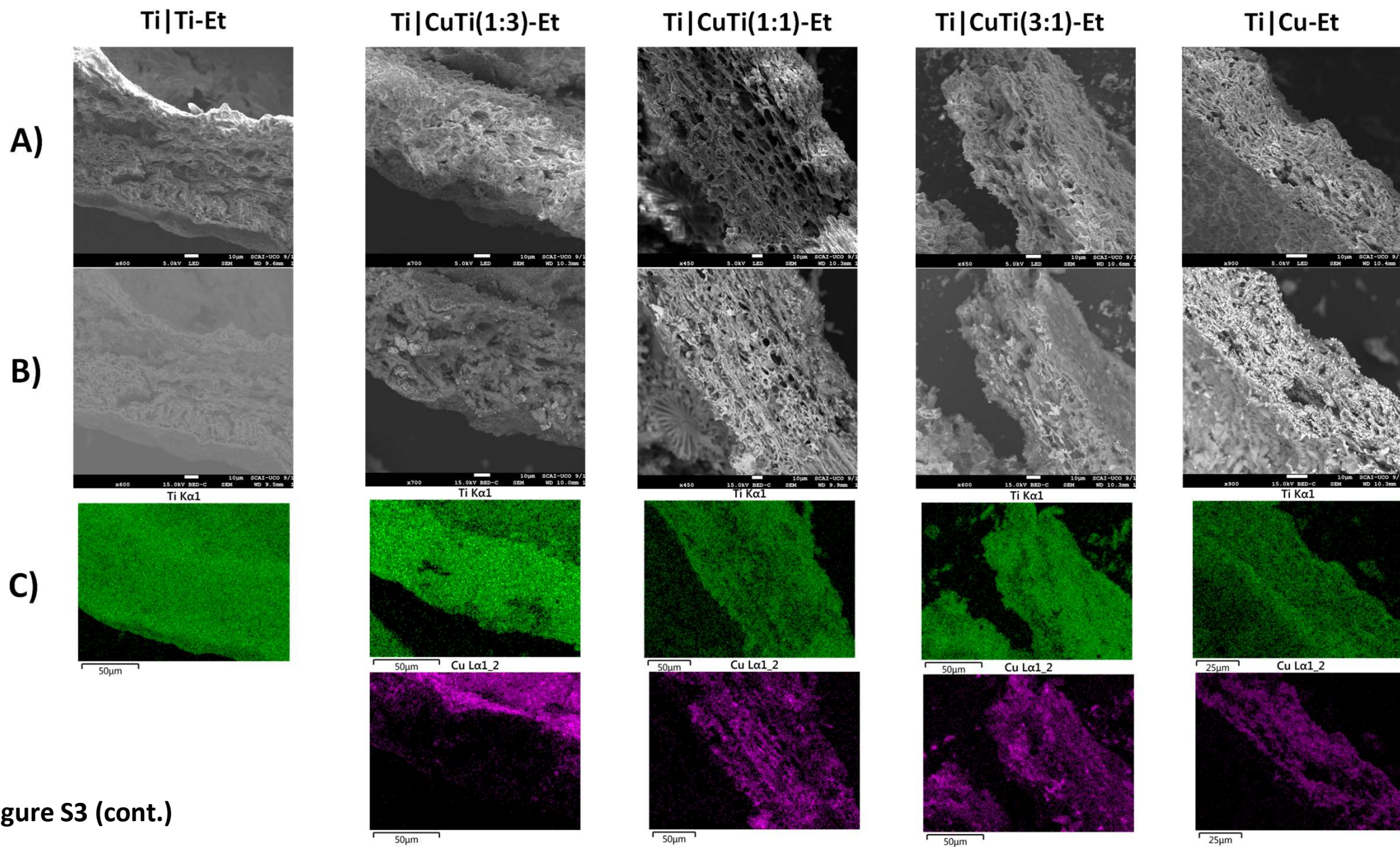
Figure S3 (cont.)
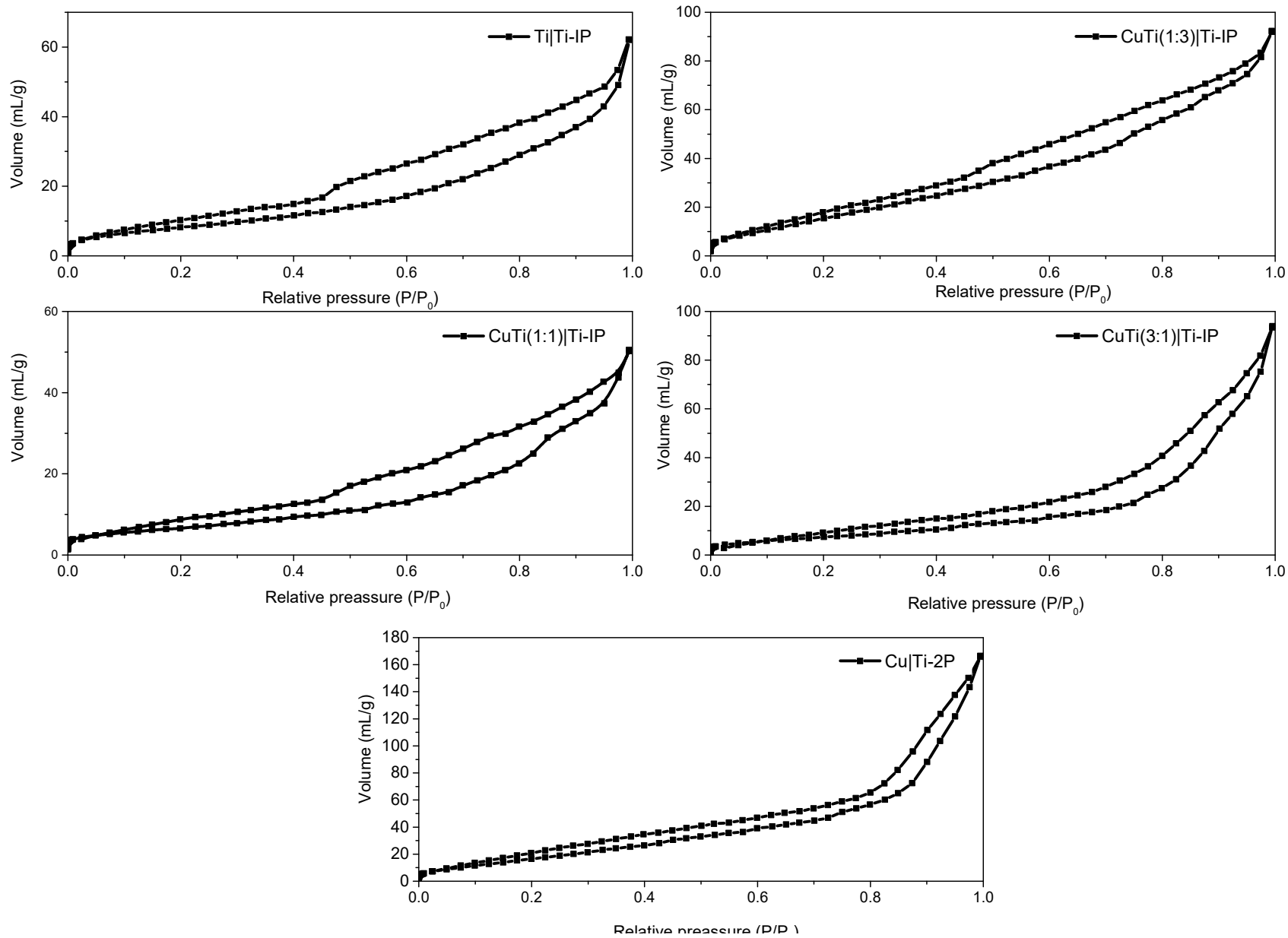
Figure S4.

Figure S4 (cont)

Figure S5